GeoSim: Photorealistic Image Simulation with Geometry-Aware Composition for Self-Driving

Yun Chen^{1*} Frieda Rong^{1,3*}, Shivam Duggal^{1*} Shenlong Wang^{1,2} Xinchen Yan¹ Sivabalan Manivasagam^{1,2} Shangjie Xue^{1,4} Ersin Yumer¹ Raquel Urtasun^{1,2} ¹Uber Advanced Technologies Group ²University of Toronto ³ Stanford University ⁴Massachusetts Institute of Technology

{chenyuntc, shivamduggal.9507, skywalkeryxc, meyumer}@gmail.com,

rongf@cs.stanford.edu, {slwang, manivasagam, urtasun}@cs.toronto.edu, sjxue@mit.edu

Abstract

Scalable sensor simulation is an important yet challenging open problem for safety-critical domains such as selfdriving. Current work in image simulation either fail to be photorealistic or do not model the 3D environment and the dynamic objects within, losing high-level control and physical realism. In this paper we present GeoSim, a geometryaware image composition process which synthesizes novel urban driving scenes by augmenting existing images with dynamic objects extracted from other scenes and rendered at novel poses. Towards this goal, we first build a diverse bank of 3D objects with both realistic geometry and appearance from sensor data. During simulation, we perform a novel geometry-aware simulation-by-composition procedure which 1) proposes plausible and realistic object placements into a given scene, 2) renders novel views of dynamic objects from the asset bank, and 3) composes and blends the rendered image segments. The resulting synthetic images are photorealistic, traffic aware, and geometrically consistent, allowing image simulation to scale to complex use cases. We demonstrate two such important applications: long-range realistic video simulation across multiple camera sensors, and synthetic data generation for data augmentation on downstream segmentation tasks.

1. Introduction

Walking along an empty pavement on a silent Sunday morning, one can easily fantasize how busy it could look during rush hour on a weekday, or how a parked car might look when driving around a different street. Humans are capable of recreating the experience of visually perceiving objects and scenes to generate new visual data in their minds. Such an ability allows us to formulate novel scenarios and synthesize events in our heads without having to experience that outcome directly.

Researchers have devoted significant effort towards enhancing computers with the capability of creating pictures by replicating visual content [62]. This brings immense value to many industries, such as film making, robot simulation, augmented reality, and teleconferencing. In the literature two main paradigms exist: *computer graphics* approaches and *image editing* methods. Computer graphics models the image generation process based on the rules of physics by creating a virtual 3D world and then mimics how light is transmitted within the world to produce a realistic scene rendering.

To produce visually appealing photo-realistic results, physics-based rendering requires a significants amount of computing resources, costly manual asset creation, and physical modeling [2]. Images produced by existing real-time rendering engines [21, 47, 19], still have a significant realism gap, reducing their impact in robot simulation and data augmentation for training. Data-driven image editing methods such as image composition [35, 39, 16, 20, 7] and generative image synthesis [65, 68, 64, 12, 32, 51] have received significant attention over the past few years. They focus on pushing realism through generative models trained from large-scale visual data. However, most of the efforts do not correspond to an underlying realistic 3D world, and as a consequence, the generated 2D contents are not directly useful for applications such as 3D gaming and robot simulation.

In this paper, we propose *GeoSim*, a realistic image manipulation framework that inserts dynamic objects into existing videos. GeoSim exploits a combination of both data-driven approaches and computer graphics, to produce low-cost asset generation and photo-realism with physically grounded simulation. In particular, by leveraging low-cost bounding box annotations and sensor data captured by a self-driving fleet driving in across multiple U.S. cities, GeoSim builds a fully-textured large-scale 3D assets bank. While self-driving

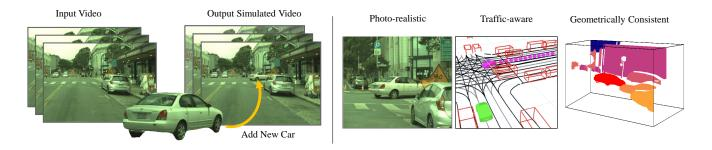


Figure 1: We proposed a novel data-driven image manipulation approach that inserts dynamic objects into existing videos. Our resulting synthetic video footages are photo-realistic, layout-aware, and geometrically consistent, allowing image simulation to scale to complex use cases.

data is widely available [23, 10, 9, 1], it is non-trivial to automatically build these assets due to the sparsity of the 3D observations, the presence of occlusions, shadows, limited viewpoints, and lighting changes. Our asset reconstruction is robust to these challenges, as we ensure consistency with multiple observations in time and learn a strong shape prior to regularize our assets. GeoSim then exploits the 3D scene layout (from high-definition (HD) maps and LiDAR readings) to add vehicles in plausible locations and make them behave realistically by considering the full scene. Finally, using this new 3D scene, GeoSim performs both imagebased rendering to properly handle occlusions, and neural network-based image inpainting to ensure the inserted object seamlessly blends in by filling holes, adjusting color inconsistencies due to lighting changes, and removing sharp boundaries.

Using GeoSim, our resulting synthetic images and video footage are photo-realistic, dynamically plausible, and geometrically consistent. We showcase two important applications: long-range realistic video simulation across multiple camera sensors and synthetic labeled data generation for training self-driving perception algorithms. Our approach outperforms prior work, in terms of both qualitative and quantitative realism metrics. We also see significant gains on perception performance when leveraging GeoSim images. These experiments suggest the potential of GeoSim for a plethora of applications, such as realistic safety verification, data augmentation, Sim2Real, augmented reality, and automatic video editing.

2. Related Work

Simulation for Robot Learning: Sensor simulation has received wide attention in the literature [56, 19, 54, 3, 57, 58, 8, 17, 67, 38, 58, 42] for its applications in training and evaluating robotic agents. Sensor simulation systems should be efficient and scalable in order to enable such applications. Many automatic approaches [57, 58, 17, 67, 38] have been proposed to generate indoor environments. Unconstrained

outdoor scenes such as the urban driving setting tackled here bring additional challenges due to the scale of the scene, weather, lighting, presence of fast moving objects, and large viewpoint changes arising from sensor motion. In the context of autonomous driving, simulation engines [19, 56, 54] based on rendered 3D models allow the combinatorial generation of scenarios with varying configurations of vehicle attributes, traffic, and weather conditions. However, these methods often have limited diversity in scene content due to the manual design of 3D assets and still have a Real2Sim gap. Data-driven sensor simulation offers a scalable alternative that can capture the complexity of the real world. Many methods [41, 22, 61, 69, 5, 46] have been proposed to directly leverage real-world data for sensor simulation in the autonomous driving domain, typically by augmenting existing recorded data to generate corresponding sensor measurements for novel scene configurations. However, previous works either focus on LiDAR [46, 22, 61], rely on CAD model registration, constraining the set of dynamic objects that can be simulated [41], or require additional effort to scale to high-resolution images [69]. In contrast, we combine data-driven simulation techniques with the image-based rendering techniques in simulation engines. This enables us to construct a scalable, geometrically consistent, and photorealistic camera simulation system.

Image Synthesis and Manipulation: Image synthesis and manipulation methods offer another route to sensor simulation. Existing work mainly focused on generating 2D images from intermediate representations including scene graphs [32, 28], surface normal maps [65], semantic segmentations [29, 74, 12, 64, 53, 51, 48], and images with different styles [34]. These methods create high-resolution images but with noticeable artifacts in texture and object shape. Rather than generating the full image in one shot, [44, 27, 40] utilize a conditional image generator for scene manipulation. In particular, [44] proposed a spatial-transformer GAN that overlays the target objects on top of existing scene layouts by iteratively adjusting 2D affine transformations. [27] in-

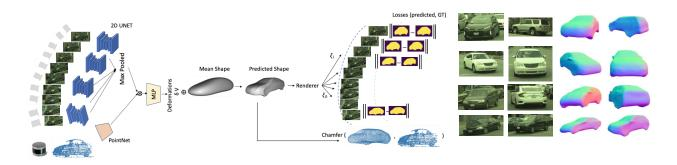


Figure 2: **Realistic 3D Assets Creation:** Left: multi-view multi-sensor reconstruction network; Right: 3D asset samples. For each sample we show one of the source images and the 3D mesh.

troduced a hierarchical image generation pipeline that is capable of inserting and removing one object at a time. This improves realism, but using purely a network-based image synthesis approach has difficulty handling complex physics such as lighting changes. [6] attempts to combine data driven approaches with graphics knowledge, using an image-based neural renderer and image decomposition to improve the synthetic result. Our work builds on this direction of leveraging graphics with real world data. We perform image-based rendering and neural in-painting to adjust for differences between the original image and the image texture of the inserted actor. Furthermore, GeoSim is aware of the 3D layout and is capable of simulating dynamic interactions between the objects and target scene.

3D Reconstruction and View Synthesis: Our neural network-based 3D asset creation step reconstructs 3D shape from camera imagery in order to synthesize novel views of dynamic objects. View synthesis and 3D reconstruction are well-studied open problems [62], with varying approaches on the relationship between geometry and appearance and possible geometric representations. Image-based rendering methods [25] focus on combining 2D textures to directly render novel views. Appearance flow-based approaches [73, 50, 60] seek to learn unconstrained pixel-level displacements, whereas [14, 75] encode geometric information in latent representations and [33] takes advantage of strong shape priors. Recently, advancements in differentiable rendering [45, 36] and open-source libraries have enabled classical graphics rendering to serve as an optimizable module, allowing for better learning of 3D and visual representations [13, 71].

3. Realistic 3D Assets Creation

In this paper we propose a novel image manipulation approach that inserts dynamic objects into an existing video footage and generates a photo-realistic video of the augmented scene that is geometrically and semantically consistent with the scene. Key to the success of such an approach is the availability of realistic 3D assets that contain accurate pose, shape and texture. Here we argue that rather than using artists to create these assets, we can leverage data captured by self-driving vehicles to reconstruct the objects around us. This is a much more scalable approach, as many self-driving datasets are available [10, 1, 23], each containing many thousands of unique assets that could potentially be reconstructed. In Sec. 3.1 we first describe how we leverage both LiDAR and camera sensor data from multiple viewpoints to generate realistic 3D vehicle assets using an asset reconstruction network. Sec. 3.2 describes our self-supervised learning procedure to train the network.

3.1. Multi-Sensor 3D Asset Reconstruction

Reconstructing 3D dynamic objects in the wild is challenging: dynamic objects are often partially observed due to the sparsity of the sensor observations and occlusions, they are seen from a limited set of viewpoints, and they appear distorted due to lighting and shadows. To tackle these challenges, we propose a novel, learning-based, multi-view, multi-sensor reconstruction approach for 3D dynamic object meshes that does not require any ground-truth 3D-shape for training. Instead, we exploit weak annotations in the form of 3D bounding boxes, which are readily available in most self-driving datasets.

More formally, let $\{\mathbf{B}_{i,j}\}_{\forall j}$ be the set of 3D bounding boxes where the i-th object is visible over j views in the recorded snippet. Let $\{\mathbf{I}_{i,j}\}_{\forall j}$ be the associated set of cropped images, and $\{\mathbf{X}_{i,j}\}_{\forall j}$ be the associated set of lidar points recorded inside $\{\mathbf{B}_{i,j}\}$, transformed to a single canonical frame and let \mathbf{X}_i be the set of aggregated LiDAR points across all views. Our 3D reconstruction network then processes the LiDAR points and image inputs in two streams that are later fused to produce the shape of the object. We refer the reader to Fig. 2 for an illustration. We represent the shape as a 3D mesh $\mathbf{M}_i = \{\mathbf{V}_i, \mathbf{F}_i\}$ where \mathbf{V}_i and \mathbf{F}_i are the faces and vertices of the mesh, respectively. In addition, we also store $\{\mathbf{I}_{i,j}, \mathbf{S}_{i,j}\}_{\forall j}$ to encode object appear-

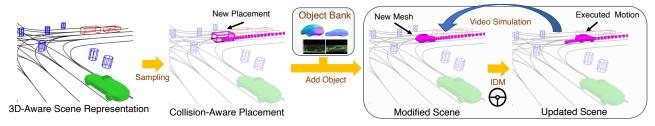


Figure 3: 3D-Aware Object Placement, Segment Retrieval, and Temporal Simulation.

ance, where $S_{i,j}$ is the extracted object's silhouette obtained from a pre-trained instance segmentation model [37]. We use this later on to perform novel-view warping.

Network Architecture: Our backbone consists of two submodules. A U-Net [55] takes each cropped camera image as input and outputs a corresponding feature map.

The feature maps from multiple cameras are then aggregated into a one-dimensional latent representation using maxpooling. A similar latent representation is extracted from the input LiDAR point cloud using a PointNet network [52]. The LiDAR and camera features are then passed through an MLP to output the final shape. Inspired by [33], we parameterize the 3D shape as a category-specific mean shape in the canonical pose and a 3D deformation per vertex. This parameterization encodes a categorical prior and ensures the completeness of the shape under partial observations.

3.2. Self-Supervised Learning

Note that we do not have supervision about the shape. We thus train our approach end-to-end in an self-supervised manner to obtain the parameters of the reconstruction network and the mean shape. Our training objective encodes the agreement between the 3D shape and the camera and LiDAR observations, as well as a regularization term.

$$\ell_{\text{total}} = \sum_{i} \{ \ell_{\text{sil}}(\mathbf{M}_{i}; \mathbf{P}_{i}, \mathbf{I}_{i}) + \ell_{\text{lidar}}(\mathbf{M}_{i}; \mathbf{X}_{i}) + \ell_{\text{reg}}(\mathbf{M}_{i}) \}$$

where *i* ranges over all the training objects. The *silhouette loss* measures the consistency between the 2D silhouette (automatically generated using the state-of-the-art object segmentation method PointRend [37]) and the silhouette of the rendered 3D shape.

$$\ell_{\rm sil}(\mathbf{M}_i; \mathbf{P}_i, \mathbf{I}_i) = \sum_j \|\mathbf{S}_{i,j} - \tau(\mathbf{M}_{\mathbf{i},\mathbf{j}}, \mathbf{P}_{\mathbf{i},\mathbf{j}})\|_2^2$$

where $\mathbf{S}_{i,j} \in \mathbb{R}^{D \times W \times H}$ is the 2D silhouette, *j* ranges over multiple views, and $\tau(\mathbf{M}, \mathbf{P})$ is a differentiable neural rendering operator [13] that renders a differentiable mask on the camera image given a projection matrix **P**. The *LiDAR loss* represents the consistency between the accumulated LiDAR point cloud and the mesh vertices, defined as the asymmetric Chamfer distance

$$\ell_{ ext{lidar}}(\mathbf{M_i}, \mathbf{X_i}) = \sum_{\mathbf{x} \in \mathbf{X}_i} \min_{\mathbf{v} \in \mathbf{V}_i} \|\mathbf{x} - \mathbf{v}\|_2^2$$

In addition, we also minimize a set of *regularizers* to enforce prior knowledge over the predicted 3D shape, namely local smoothness on the vertices as well as normals. This includes 1) a Laplacian regularization which preserves local geometry and prevents intersecting faces; 2) mesh normal regularization which enforces smoothness of local surfaces; 3) edge regularization which penalizes long edges. Please refer to supplementary material for details.

4. Geometry-Aware Image Simulation

Here we describe our image simulation by composition approach that places novel objects into an existing 3D scene and generates a photo-realistic video sequence of the composition. Our approach takes as input camera video footage, LiDAR point clouds, and an HD map in the form of a lane graph and automatically outputs a photo-realistic video with novel objects inserted into the scene. Note that the input sensory data and HD maps we employ are readily available in most self-driving platforms, which are the application domain we tackle in this paper. Importantly, our simulation takes into account both geometric occlusions by other actors and the background, plausibility of the locations and motions as well as the interactions with other dynamic agents and thus avoids collision for the newly inserted objects.

Towards this goal, we first infer the location of all objects in the scene by performing 3D object detection and tracking [43]. For each new object to be inserted we select where to place it as well as which asset to use based on the HD map and the existing detected traffic. We then utilize an intelligent traffic model for our newly place object such that its motion is realistic, takes into account the interactions with other actors and avoids collision. The output of this process defines the new scenario to be rendered. We then use a novel-view rendering with 3D occlusion reasoning w.r.t. all elements in the scene, to create the appearance of the novel objects in the new image. Finally, we utilize a neural network to fill in the boundary of the inserted objects, create any missing texture and handle inconsistent lighting. Fig. 1 outlines our approach.

4.1. Scenario Generation

We want to place new objects in existing images such that they are plausible in terms of their scale, location, orientation and motion. Towards this goal, we design a 3D sampling procedure, which takes advantage of the priors we have about how vehicles behave in our cities. Note that achieving similar levels of realism would be extremely difficult to capture in the 2D world. We thus exploit HD maps that contain the location of the lanes in bird's eye view (BEV), and parameterize the object placement as a tuple (x, y, θ) defining the object center and orientation in BEV, which we later convert to a 6DoF pose using the local ground elevation.

Note that our object samples should have realistic physical interactions with existing objects, respect the flow of traffic, and be visible in the camera's field of view. To achieve this, we randomly sample a placement (x, y) from the lane regions lying within the camera's field of view and retrieve the orientation from the lane. We reject all samples that result in collision with other actors or background objects. The aforementioned process provides the placement of the object in the initial frame. In order to simulate plausible placements over time for video simulation, we use the Intelligent Driver Model (IDM) [59] fitted to a kinematic model following [24], to update the simulated object's state for realistic interactions with surrounding traffic. IDM is a continuous-time car-following model that controls the longitudinal dynamics of the car, ensures a safe braking distance, and has comfortable braking/acceleration. Fig. 3 depicts the full procedure of placement and kinematics simulation.

So far we have selected where to place an object and how is going to move, but we still need to select which object to place. In order to minimize the artifacts when rendering our assets, we propose to retrieve objects from the asset bank that were viewed with similar viewpoints and distance to the camera in the original footage. The former avoids the need to deal with large unseen object regions while the latter avoids utilizing assets that have been captured at lower resolution. Please refer to the supplementary material for the specific scoring criteria. Objects are then sampled (as opposed to a hard max) according to a categorical distribution weighted by their inverse score. Once a segment is retrieved for a desired placement, we perform collision checking using the retrieved object shape to ensure that the placement is valid.

4.2. Occlusion-Aware Neural Rendering

Now that we have selected a source object and its corresponding camera image based on the segment retrieval mechanism defined above, we proceed to render this source object into the target scene. Since the object's target pose might differ from the original observed poses, we cannot simply paste the image segment from the source to the target. Thus we proposed to utilize the asset's 3D shape to warp the source to the novel target view.

Novel-view Warping: Let M be the selected object's 3D mesh, I_s be the source object's camera image, and P_s/P_t be the source/ target camera matrices. We first render M_s at the selected target viewpoint to generate the corresponding target depth map, D_t . Then using the rendered depth map and source camera image I_s , we generate the object's 2D texture map using the inverse warping operation [63, 30] as:

$$\mathbf{I}_{t} = \mathbf{I}_{s}(\pi(\pi^{-1}(\mathbf{D}_{t}, \mathbf{P}_{t}), \mathbf{P}_{s})) \text{, where } \mathbf{D}_{t} = \psi(\mathbf{M}, \mathbf{P}_{t}),$$

 ψ is a differentiable neural renderer [13] that produces a depth image given the 3D mesh M and camera matrix P; π is the perspective projection and π^{-1} is the inverse projection that takes the depth image and camera matrix as input and outputs the 3D points.

Shadow Generation: Inserting an object into a scene will not only result in changes to the pixels where the object is present, but can also change the rest of the scene (i.e. shadows and ambient occlusion). We improve the perceptual quality of the image by approximating these effects with image based rendering. To estimate the shadow casted by each inserted object, we construct a virtual scene with the inserted object and a ground plane and exploit image-based rendering [18], where the environment light comes from a real-world HDRI. We render the scene with and without the inserted objects, and add the shadow by blending in the background image intensities with the ratio of the two rendered images intensities. For simplicity, we select a cloudy HDRI to cast shadows. In practice, we find this produces reasonable results.

Occlusion Reasoning: An inserted object must respect occlusions from the existing scene elements. Vegetation, fences, and other dynamic objects, for example, may have irregular or thin boundaries, complicating occlusion reasoning. We employ a simple strategy to determine occlusions of the inserted objects and their shadow in the target scene by comparing their depth w.r.t the depth map of the existing 3D scene. To achieve this, we first estimate the target image's dense depth map through a depth completion network [15]. The input is the RGB image and a sparse depth map acquired by projecting the LiDAR sweep onto the image. Using the rendered depth of the object, the occlusion mask is then computed by evaluating for each object pixel if the target image's depth is smaller than the corresponding object pixel's depth.

Post-Composition Synthesis: After occlusion reasoning, the rendered image may still look unrealistic as the in-

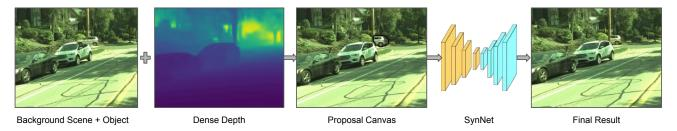


Figure 4: Geometry-aware composition with occlusion reasoning followed by an image synthesis module.

Method	Human Score	FID
SPADE [51]	99.3	43.20
Guided Editing [27]	94.3	20.33
Cut-Paste [20]	98.50	22.07
CAD [3]	94.28	17.32
GeoSim	-	14.33

Table 1: **Perceptual Quality Evaluation:** Human score: Percentage of participants who prefers our GeoSim results over baseline method. FID score: Fréchet Inception Distance between synthesized images and real images (lower is better).

serted segment may have inconsistent illumination and colorbalancing w.r.t the target scene, discrepancies at the boundaries, and missing regions that were not available in the source view. To solve these issues, we leverage an image synthesis network to naturally blend the source segment to the target scene (see Fig. 4). Our network takes the target background image \mathbf{B}_t , masked target object rendering \mathbf{I}_t as well as the object binary silhouette S_t as input, and outputs the final image that naturally composites the background and rendered object. Our synthesis network architecture is similar to [70], which is a generative image inpainting network except that we take the rendered object mask as additional input. Our network is trained using images with instance segmentation masks inferred by [37] in the target scene. Data augmentation, including random occlusion, color jittering, as well as random contrast and saturation is applied to mimic the differences among real-world images. Two loss functions are adopted, namely the perceptual loss [31] to ensure the generated output's fidelity, as well as a GAN loss to boost the realism of the inpainted region as well as the lighting consistency. Please refer to the supplementary material for more details.

5. Experimental Evaluation

In this section we first introduce our experimental setting. We then compare GeoSim against a comprehensive set of image simulation baselines in visual realism through perceptual quality scores and human A/B tests, and in downstream tasks such as semantic segmentation. We also showcase our method generating multi-camera and temporally consistent video simulation. While our method can be adapted to handle most rigid objects, in our experiments we showcase vehicles, the most common and relevant objects in self driving.

5.1. Experimental Details

We utilize two large-scale self-driving datasets (Urban-Data and Argoverse [10]) to showcase GeoSim.

UrbanData: We collected a real-world dataset by having a fleet of self-driving cars drive in two major cities in North America. We labeled 16,500 snippets, where each snippet contains 25 seconds (~250 frames, sampled at 10Hz) of video with 7 cameras, a 64-beam LiDAR sensor, and HD maps. We use 4500 for reconstruction and synthesis network training, 7000 for depth completion training, and 5000 for perceptual quality and downstream evaluation. Please see supplementary for the full breakdown.

Argoverse: We also evaluate on the Argoverse training split which contains 65 snippets from 2 different cities. We use the provided HD maps for vehicle placement. We directly adopt the 3D assets built from UrbanData, as Argoverse is too small for diverse assets creation. We train our image synthesis network on Argoverse, where 80,000 frames are sampled for training and 15,915 are sampled for evaluation.

Asset Bank Creation: We created automatically a large object bank of ~ 8000 vehicles, from cameras, LiDAR data and 3D bounding boxes using our 3D reconstruction network on UrbanData. Each successfully reconstructed object is registered in our 3D asset bank, with its 1) 3D mesh; 2) images; and 3) object pose in ego-vehicle-centric coordinates. We use a pre-trained instance segmentation to get the inferred instance mask [37], a LiDAR detector [43] to acquire other actors' bounding boxes for collision avoidance (Sec. 4.1), and a depth completion network [15] to get dense depth for occlusion reasoning (Sec. 4.2).



Figure 5: Qualitative Comparison of Image Simulation approaches.

Baselines: We compare our method against several deep learning based end-to-end 2D image synthesis and augmentation baselines [40, 64, 27, 51]. Unlike GeoSim, these methods cannot perform placement directly and require an input mask based on the objectss' shape and pose that denote the area to synthesize. We therefore use [40] to insert object instances at the semantic level in a background semantic image. We then generate high resolution images from this augmented scene representation with three different approaches: (1) Holistic image generation ("SPADE"): we use the stateof-the-art conditional image generation model SPADE [51] to generate the entire image given the semantic mask. (2) Retrieval-based generation ("Cut-Paste"): given the new object's 2D mask, we retrieve the most similar example from a bank of 2D object images. The similarity is defined using semantic mask IOU. The rest of the background comes from the corresponding real image; and (3) Guided semantic image editing ("Guided-Editing"): we use [27] to inpaint the tight bounding box region of the added object. Additionally, we compare against a graphics-based CAD model insertion baseline ("CAD"), in spirit of [4] with the following differences: 1) we use our 3D placement in order to produce more realistic layout-aware insertion; 2) unlike the original work, we do not have environment light for both datasets, and thus use a HDRI captured at a cloudy day instead.

5.2. Perceptual Quality Evaluation

Human Study: To verify the realism of our approach, we conduct a human A/B test, where we show a pair of images generated from different approaches on the same background image, one from GeoSim and another one from a competing algorithm. We then ask the human judges to click the one they believe is more realistic. In total, 13 human judges participated and labeled ~ 1500 image pairs. Tab. 1 shows the human preference score for each algorithm, which mea-

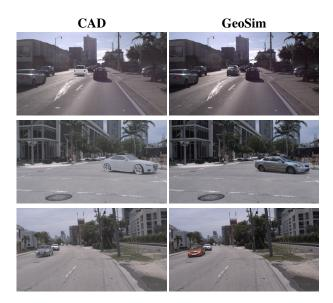


Figure 6: Qualitative Comparison of Image Simulation approaches in Argoverse.

sures the percentage of participants who prefers our GeoSim results over each baseline method. Results on Argoverse are presented in Tab. 4. The A/B test confirms that our method produces drastically more realistic images than the baselines. Please see the detailed interface and instructions on A/B test in supplementary material.

Perceptual Quality Score: We further use the Fréchet Inception Distance (FID) [26] between the synthesized images and the ground-truth images as an automatic measure of image quality. We report the FID on the full image for GeoSim and the baselines in Tab. 1. Our method significantly outperforms all competing methods on FID.

Method	PSPNet [72]		DeepLa	ıbv3 [11]
	mIOU	carIOU	mIOU	carIOU
Real	93.47	87.84	93.96	88.74
Real+GeoSim	95.30	91.22	94.18	89.15

Table 2: Sim2Real on Semantic Segmentation.

Approach	Shadow	Human Score	FID
Physics	Yes	94.2	17.32
2D Synthesis	-	75.7	13.74
Geo Synthesis	No	71.9	13.72
Geo Synthesis	Yes	-	14.33

Table 3: **Ablation on Rendering Options for GeoSim.** Human score: Percentage of participants who prefers our GeoSim results over baseline method. FID score: Fréchet Inception Distance between synthesized images and real images (lower is better).

Qualitative Comparison: Fig. 5 shows representative simulated images. Note that GeoSim is significantly more realistic than the baselines. While one can easily and quickly detect the added object in other methods due to unrealistic generation creating smeared cars ("SPADE", "Guided-Editing"), or geometrically invalid results ("Cut-Paste"), or unrealistic appearance ("CAD"), one must look closely at GeoSim images to distinguish the added object from the real ones. We also show qualitative examples of GeoSim in Argoverse in Fig. 6, where we obtain very high visual quality. This demonstrates GeoSim's good potential to generalize across datasets. GeoSim has some failure modes caused by unnatural boundaries or incorrect occlusion reasoning when adding the new object (see supplementary for qualitative cases).

Effect of Rendering Approach: We evaluate the importance of using a hybrid rendering module proposed in our method, compared to using solely physics-based rendering or 2D synthesis with 3D placement constant across all approaches). As shown in Tab. 3, our proposed geometry-aware synthesis significantly outperforms all other approaches on human scores. Additionally, enhancing hybrid-rendering with shadows significantly boosts the realism for humans, but such improvements are not reflected in FID score. This suggests there still exists a gap between computational perceptual quality measurements and humans' criteria.

Video Simulation: We also showcase in the supplementary video GeoSim's ability to simulate photorealistic and temporally consistent video for multiple cameras.

Method	Human Score	FID
CAD	84.00	28.26
GeoSim	-	24.54

Table 4: **Results on Argoverse.** Human score: Percentage of participants who prefers our GeoSim results over baseline method. FID score: Fréchet Inception Distance between synthesized images and real images (lower is better).

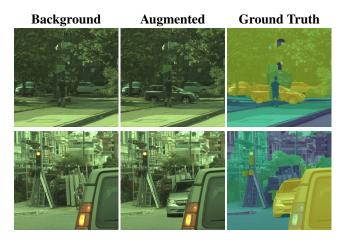


Figure 7: GeoSim for data augmentation. Left: Before augmentation. Middle: After augmentation. Right: Augmented semantic ground truth.

5.3. Downstream Perception Task

We now investigate data augmentation, where we use a small amount of labeled real data combined with GeoSim to get significance performance gains, without the cost of large scale annotations (as seen in Fig. 7). We first train a segmentation model on a small amount of labeled real data with around 2000 images. We then use GeoSim to augment these images with inserted vehicles, obtaining 9879 additional training examples in total. We re-train the segmentation model on both real and augmented data for the same number of iterations. We evaluate the performance on real data and report the results on Tab. 2. With these additional training images, we can further boost perception performance by 3.4% (or 0.4% on DeepLabv3 [11]) for car category and 1.8% (or 0.2% on DeepLabv3 [11]) for overall mIOU on PSPNet [72]. Importantly we can show consistent improvements across two segmentation models.

6. Conclusion

In this work we presented a novel geometry-guided simulation procedure for flexible generation and rendering of synthetic scenes. Not only is our approach the first of its kind to fully take into consideration physical realism for dynamic object placement into images, it also bypasses the need for manual 3D asset creation and achieves greater visual realism than competing alternatives. Moreover we demonstrated improvements in downstream tasks through applications of our technique to semantic segmentation. There are many exciting follow-up directions opened up by this work such as sim2real, autonomous system verification and evaluation, video editing, *etc.* and we look forward to future extensions of GEOSIM.

References

- [1] Waymo open dataset: An autonomous driving dataset, 2019.2, 3
- [2] Corona renderer, 2020. 1
- [3] Hassan Abu Alhaija, Siva Karthik Mustikovela, Lars Mescheder, Andreas Geiger, and Carsten Rother. Augmented Reality Meets Computer Vision : Efficient Data Generation for Urban Driving Scenes. arXiv, 2017. 2, 6
- [4] Hassan Abu Alhaija, Siva Karthik Mustikovela, Lars Mescheder, Andreas Geiger, and Carsten Rother. Augmented reality meets computer vision: Efficient data generation for urban driving scenes. *International Journal of Computer Vision*, 2018. 7
- [5] Alexander Amini, Igor Gilitschenski, Jacob Phillips, Julia Moseyko, Rohan Banerjee, Sertac Karaman, and Daniela Rus. Learning Robust Control Policies for End-to-End Autonomous Driving From Data-Driven Simulation. *IEEE Robotics and Automation Letters*, 2020. 2
- [6] Anonymous. Cut-and-paste neural rendering. In Submitted to International Conference on Learning Representations, 2021. under review. 3
- [7] Anand Bhattad and David A Forsyth. Cut-and-paste neural rendering. *arXiv preprint arXiv:2010.05907*, 2020. 1
- [8] Konstantinos Bousmalis, Alex Irpan, Paul Wohlhart, Yunfei Bai, Matthew Kelcey, Mrinal Kalakrishnan, Laura Downs, Julian Ibarz, Peter Pastor, Kurt Konolige, et al. Using simulation and domain adaptation to improve efficiency of deep robotic grasping. In *ICRA*, 2018. 2
- [9] Holger Caesar, Varun Bankiti, Alex H. Lang, Sourabh Vora, Venice Erin Liong, Qiang Xu, Anush Krishnan, Yu Pan, Giancarlo Baldan, and Oscar Beijbom. nuscenes: A multimodal dataset for autonomous driving. *arXiv*, 2019. 2
- [10] Ming-Fang Chang, John W Lambert, Patsorn Sangkloy, Jagjeet Singh, Slawomir Bak, Andrew Hartnett, De Wang, Peter Carr, Simon Lucey, Deva Ramanan, and James Hays. Argoverse: 3d tracking and forecasting with rich maps. In *CVPR*, 2019. 2, 3, 6
- [11] Liang-Chieh Chen, George Papandreou, Florian Schroff, and Hartwig Adam. Rethinking atrous convolution for semantic image segmentation. *arXiv preprint arXiv:1706.05587*, 2017. 8, 13
- [12] Qifeng Chen and Vladlen Koltun. Photographic Image Synthesis with Cascaded Refinement Networks. *arXiv*, 2017. 1, 2
- [13] Wenzheng Chen, Jun Gao, Huan Ling, Edward Smith, Jaakko Lehtinen, Alec Jacobson, and Sanja Fidler. Learning to predict 3d objects with an interpolation-based differentiable renderer. In *NIPS*, 2019. 3, 4, 5

- [14] Xu Chen, Jie Song, and Otmar Hilliges. Monocular Neural Image Based Rendering with Continuous View Control. arXiv, 2019. 3
- [15] Yun Chen, Bin Yang, Ming Liang, and Raquel Urtasun. Learning joint 2d-3d representations for depth completion. In *ICCV*, 2019. 5, 6
- [16] Wenyan Cong, Jianfu Zhang, Li Niu, Liu Liu, Zhixin Ling, Weiyuan Li, and Liqing Zhang. Dovenet: Deep image harmonization via domain verification. In Proceedings of the IEEE/CVF Conference on Computer Vision and Pattern Recognition, pages 8394–8403, 2020. 1
- [17] Erwin Coumans and Yunfei Bai. Pybullet, a python module for physics simulation for games, robotics and machine learning. *GitHub repository*, 2016. 2
- [18] Paul Debevec. Rendering synthetic objects into real scenes: Bridging traditional and image-based graphics with global illumination and high dynamic range photography. In ACM SIGGRAPH 2008 classes, pages 1–10. 2008. 5
- [19] Alexey Dosovitskiy, German Ros, Felipe Codevilla, Antonio Lopez, and Vladlen Koltun. CARLA: An Open Urban Driving Simulator. 2017. 1, 2
- [20] Debidatta Dwibedi, Ishan Misra, and Martial Hebert. Cut, paste and learn: Surprisingly easy synthesis for instance detection. In *Proceedings of the IEEE International Conference* on Computer Vision, pages 1301–1310, 2017. 1, 6
- [21] Epic Games. Unreal engine. 1
- [22] Jin Fang, Dingfu Zhou, Feilong Yan, Tongtong , Feihu Zhang, Yu Ma, Liang Wang, and Ruigang Yang. Augmented LiDAR Simulator for Autonomous Driving. arXiv, 2019. 2
- [23] Andreas Geiger, Philip Lenz, Christoph Stiller, and Raquel Urtasun. Vision meets robotics: The kitti dataset. *International Journal of Robotics Research (IJRR)*, 2013. 2, 3
- [24] J. Gonzales, Fan Zhang, Keqiang Li, and Francesco Borrelli. Autonomous drifting with onboard sensors. 2016. 5
- [25] Peter Hedman, Julien Philip, True Price, Jan-Michael Frahm, George Drettakis, and Gabriel Brostow. Deep blending for free-viewpoint image-based rendering. 2018. 3
- [26] Martin Heusel, Hubert Ramsauer, Thomas Unterthiner, Bernhard Nessler, and Sepp Hochreiter. Gans trained by a two time-scale update rule converge to a local nash equilibrium. 2017. 7
- [27] Seunghoon Hong, Xinchen Yan, Thomas Huang, and Honglak Lee. Learning Hierarchical Semantic Image Manipulation through Structured Representations. arXiv, 2018. 2, 6, 7
- [28] Seunghoon Hong, Dingdong Yang, Jongwook Choi, and Honglak Lee. Inferring semantic layout for hierarchical textto-image synthesis. In CVPR, 2018. 2
- [29] Phillip Isola, Jun-Yan Zhu, Tinghui Zhou, and Alexei A Efros. Image-to-image translation with conditional adversarial networks. In CVPR, 2017. 2
- [30] Max Jaderberg, Karen Simonyan, Andrew Zisserman, and Koray Kavukcuoglu. Spatial Transformer Networks. *arXiv*, 2016. 5
- [31] Justin Johnson, Alexandre Alahi, and Fei-Fei Li. Perceptual losses for real-time style transfer and super-resolution. *CoRR*, 2016. 6, 14

- [32] Justin Johnson, Agrim Gupta, and Li Fei-Fei. Image generation from scene graphs. In CVPR, 2018. 1, 2
- [33] Angjoo Kanazawa, Shubham Tulsiani, Alexei A. Efros, and Jitendra Malik. Learning Category-Specific Mesh Reconstruction from Image Collections. *arXiv*, 2018. 3, 4
- [34] Tero Karras, Samuli Laine, and Timo Aila. A style-based generator architecture for generative adversarial networks. In *CVPR*, 2019. 2
- [35] Kevin Karsch, Varsha Hedau, David Forsyth, and Derek Hoiem. Rendering synthetic objects into legacy photographs. *ACM Transactions on Graphics (TOG)*, 30(6):1–12, 2011. 1
- [36] Hiroharu Kato, Yoshitaka Ushiku, and Tatsuya Harada. Neural 3D Mesh Renderer. *arXiv*, 2017. 3
- [37] Alexander Kirillov, Yuxin Wu, Kaiming He, and Ross Girshick. Pointrend: Image segmentation as rendering. In *CVPR*, 2020. 4, 6, 14, 16
- [38] Eric Kolve, Roozbeh Mottaghi, Winson Han, Eli VanderBilt, Luca Weihs, Alvaro Herrasti, Daniel Gordon, Yuke Zhu, Abhinav Gupta, and Ali Farhadi. Ai2-thor: An interactive 3d environment for visual ai. arXiv, 2017. 2
- [39] Jean-François Lalonde, Derek Hoiem, Alexei A Efros, Carsten Rother, John Winn, and Antonio Criminisi. Photo clip art. ACM transactions on graphics (TOG), 26(3):3–es, 2007. 1
- [40] Donghoon Lee, Sifei Liu, Jinwei Gu, Ming-Yu Liu, Ming-Hsuan Yang, and Jan Kautz. Context-aware synthesis and placement of object instances. In *NIPS*, 2018. 2, 7
- [41] Wei Li, Chengwei Pan, Rong Zhang, Jiaping Ren, Yuexin Ma, Jin Fang, Feilong Yan, Qichuan Geng, Xinyu Huang, Huajun Gong, Weiwei Xu, Guoping Wang, Dinesh Manocha, and Ruigang Yang. AADS: Augmented Autonomous Driving Simulation using Data-driven Algorithms. *Science Robotics*, 2019. 2
- [42] Xueting Li, Sifei Liu, Kihwan Kim, Xiaolong Wang, Ming-Hsuan Yang, and Jan Kautz. Putting humans in a scene: Learning affordance in 3d indoor environments. In CVPR, 2019. 2
- [43] Ming Liang, Bin Yang, Wenyuan Zeng, Yun Chen, Rui Hu, Sergio Casas, and Raquel Urtasun. Pnpnet: End-to-end perception and prediction with tracking in the loop. In *CVPR*, 2020. 4, 6, 16
- [44] Chen-Hsuan Lin, Ersin Yumer, Oliver Wang, Eli Shechtman, and Simon Lucey. ST-GAN: Spatial Transformer Generative Adversarial Networks for Image Compositing. arXiv, 2018. 2
- [45] Shichen Liu, Tianye Li, Weikai Chen, and Hao Li. Soft Rasterizer: A Differentiable Renderer for Image-based 3d Reasoning. arXiv, 2019. 3
- [46] Sivabalan Manivasagam, Shenlong Wang, Kelvin Wong, Wenyuan Zeng, Mikita Sazanovich, Shuhan Tan, Bin Yang, Wei-Chiu Ma, and Raquel Urtasun. Lidarsim: Realistic lidar simulation by leveraging the real world. *CVPR*, 2020. 2
- [47] Mark Martinez, Chawin Sitawarin, Kevin Finch, Lennart Meincke, Alex Yablonski, and Alain Kornhauser. Beyond grand theft auto v for training, testing and enhancing deep learning in self driving cars. arXiv, 2017. 1
- [48] Sangwoo Mo, Minsu Cho, and Jinwoo Shin. Instagan: Instance-aware image-to-image translation. *arXiv*, 2018. 2

- [49] Andrew Nealen, Takeo Igarashi, Olga Sorkine, and Marc Alexa. Laplacian mesh optimization. 2006. 12
- [50] Eunbyung Park, Jimei Yang, Ersin Yumer, Duygu Ceylan, and Alexander C. Berg. Transformation-Grounded Image Generation Network for Novel 3d View Synthesis. *arXiv*, 2017. 3
- [51] Taesung Park, Ming-Yu Liu, Ting-Chun Wang, and Jun-Yan Zhu. Semantic image synthesis with spatially-adaptive normalization. In *CVPR*, 2019. 1, 2, 6, 7
- [52] Charles R Qi, Hao Su, Kaichun Mo, and Leonidas J Guibas. Pointnet: Deep learning on point sets for 3d classification and segmentation. arXiv, 2016. 4, 12
- [53] Xiaojuan Qi, Qifeng Chen, Jiaya Jia, and Vladlen Koltun. Semi-parametric Image Synthesis. arXiv, 2018. 2
- [54] Stephan R. Richter, Vibhav Vineet, Stefan Roth, and Vladlen Koltun. Playing for Data: Ground Truth from Computer Games. arXiv, 2016. 2
- [55] Olaf Ronneberger, Philipp Fischer, and Thomas Brox. U-net: Convolutional networks for biomedical image segmentation. *CoRR*, 2015. 4
- [56] German Ros, Laura Sellart, Joanna Materzynska, David Vazquez, and Antonio M Lopez. The synthia dataset: A large collection of synthetic images for semantic segmentation of urban scenes. In *CVPR*, 2016. 2
- [57] Manolis Savva, Angel X Chang, Alexey Dosovitskiy, Thomas Funkhouser, and Vladlen Koltun. Minos: Multimodal indoor simulator for navigation in complex environments. arXiv, 2017. 2
- [58] Manolis Savva, Abhishek Kadian, Oleksandr Maksymets, Yili Zhao, Erik Wijmans, Bhavana Jain, Julian Straub, Jia Liu, Vladlen Koltun, Jitendra Malik, et al. Habitat: A platform for embodied ai research. In *ICCV*, 2019. 2
- [59] Jens Schulz, Constantin Hubmann, Julian Löchner, and Darius Burschka. Interaction-Aware Probabilistic Behavior Prediction in Urban Environments. arXiv, 2018. 5, 15
- [60] Shao-Hua Sun, Minyoung Huh, Yuan-Hong Liao, Ning Zhang, and Joseph J. Lim. Multi-view to Novel View: Synthesizing Novel Views With Self-learned Confidence. In ECCV. 2018. 3
- [61] Abhijeet Tallavajhula, Cetin Mericli, and Alonzo Kelly. Offroad lidar simulation using data driven terrain primitives. In *ICRA*, 2018. 2
- [62] Ayush Tewari, Ohad Fried, Justus Thies, Vincent Sitzmann, Stephen Lombardi, Kalyan Sunkavalli, Ricardo Martin-Brualla, Tomas Simon, Jason Saragih, Matthias Nießner, Rohit Pandey, Sean Fanello, Gordon Wetzstein, Jun-Yan Zhu, Christian Theobalt, Maneesh Agrawala, Eli Shechtman, Dan B. Goldman, and Michael Zollhöfer. State of the Art on Neural Rendering. arXiv, 2020. 1, 3
- [63] Shubham Tulsiani, Richard Tucker, and Noah Snavely. Layerstructured 3d scene inference via view synthesis. In ECCV, 2018. 5
- [64] Ting-Chun Wang, Ming-Yu Liu, Jun-Yan Zhu, Andrew Tao, Jan Kautz, and Bryan Catanzaro. High-Resolution Image Synthesis and Semantic Manipulation with Conditional GANs. arXiv, 2017. 1, 2, 7

- [65] Xiaolong Wang and Abhinav Gupta. Generative image modeling using style and structure adversarial networks. In ECCV, 2016. 1, 2
- [66] Yuxin Wu and Kaiming He. Group normalization. In *ECCV*, 2018. 12
- [67] Fei Xia, Amir R. Zamir, Zhiyang He, Alexander Sax, Jitendra Malik, and Silvio Savarese. Gibson Env: Real-World Perception for Embodied Agents. In *CVPR*, 2018. 2
- [68] Chao Yang, Xin Lu, Zhe Lin, Eli Shechtman, Oliver Wang, and Hao Li. High-Resolution Image Inpainting using Multi-Scale Neural Patch Synthesis. arXiv, 2016. 1
- [69] Zhenpei Yang, Yuning Chai, Dragomir Anguelov, Yin Zhou, Pei Sun, Dumitru Erhan, Sean Rafferty, and Henrik Kretzschmar. SurfelGAN: Synthesizing Realistic Sensor Data for Autonomous Driving. arXiv, 2020. 2
- [70] Jiahui Yu, Zhe Lin, Jimei Yang, Xiaohui Shen, Xin Lu, and Thomas Huang. Free-Form Image Inpainting with Gated Convolution. arXiv, 2019. 6, 14
- [71] Yuxuan Zhang, Wenzheng Chen, Huan Ling, Jun Gao, Yinan Zhang, Antonio Torralba, and Sanja Fidler. Image gans meet differentiable rendering for inverse graphics and interpretable 3d neural rendering. arXiv preprint arXiv:2010.09125, 2020. 3
- [72] Hengshuang Zhao, Jianping Shi, Xiaojuan Qi, Xiaogang Wang, and Jiaya Jia. Pyramid scene parsing network. In *CVPR*, 2017. 8
- [73] Tinghui Zhou, Shubham Tulsiani, Weilun Sun, Jitendra Malik, and Alexei A. Efros. View Synthesis by Appearance Flow. *arXiv*, 2016. 3
- [74] Jun-Yan Zhu, Taesung Park, Phillip Isola, and Alexei A Efros. Unpaired image-to-image translation using cycle-consistent adversarial networks. In *ICCV*, 2017. 2
- [75] Jun-Yan Zhu, Zhoutong Zhang, Chengkai Zhang, Jiajun Wu, Antonio Torralba, Joshua B. Tenenbaum, and William T. Freeman. Visual Object Networks: Image Generation with Disentangled 3D Representation. arXiv, 2018. 3

Appendix

In this supplementary material, we first describe additional technical details on 3D reconstruction, semantic retrieval, depth completion, post-composition, video simulation, dataset breakdown as well as A/B human test design (Sec. 1). Furthermore, we provide an extensive collection of qualitative results on comparisons, qualitative ablation on different modules of post-synthesis, and failure case analysis (Sec. 2). Finally, we recommend the reviewers to watch our HD supplementary video (supp_video.mp4), which contains an overview of our approach and video simulation results.

A. Additional Technical Details

A.1. 3D Reconstruction Network

Our 3D reconstruction network takes cropped images and LiDAR sweeps from multiple viewpoints. All cropped images are padded to have the same height and width and are then resized to 256×256 . A small fully convolution network (as seen in Fig. 8) is used to extract image features. Note that in the figure, Conv(K, S, C) refers to a convolution layer with kernel size K, stride S and output channel C. Padding is adjusted to make sure the output size is the same as the input. GroupNorm [66] with 32 channels per group is used after each convolution. ReLU is used as the non-linear activation. The final output is flattened to a single feature vector for each image.

To fuse the image features from multiple views, we design a fuse block (as shown on the right of Fig 8). In the block, multiview features are maxpooled to a single vector, which is then concatenated with each input. The augmented feature vector for each view is processed by a two layer MLP. The dimensions of all hidden layers and output layers of the MLP are 1024. We adopt 4 fuse blocks and maxpool to generate the final image-based feature vector. We adopt a standard PointNet [52] as the LiDAR feature extractor, which produces a feature vector with size 1024. Two linear layers consume the final concatenated LiDAR and image features to produce the mean-shape mesh deformation δV . The mean-shape mesh is initialized from an icosasphere with 2562 vertices and 5120 triangle faces.

As defined in the paper, we supervise the mesh reconstruction pipeline using silhoutte consistency loss, LiDAR consistency loss and the mesh regularization terms. The *regularizers* are applied to enforce prior knowledge over the resultant 3D shape, namely local smoothness on the vertices as well as normals.

$$\ell_{\text{regularization}}(\mathbf{M}_i) = \alpha \ell_{\text{edge}}(\mathbf{M}_i) + \beta \ell_{\text{normal}}(\mathbf{M}_i) + \gamma \ell_{\text{laplacian}}(\mathbf{M}_i)$$

The *edge regularization* term penalizes long edges, thereby preventing isolated vertices. $\ell_{edge}(\mathbf{M}_i) = \sum_{\mathbf{v} \in \mathbf{V}_i} \sum_{\mathbf{v}' \in \mathbf{N}_v} \|\mathbf{v} - \mathbf{v}'\|_2^2$, with \mathbf{N}_v the first ring neighbour vertices of a given vertex \mathbf{v} . The *Laplacian regularization* [49] preserves local geometry and prevents intersecting mesh faces by encouraging the centroid of the neighbouring vertices to be close to the vertex: $\ell_{laplacian}(\mathbf{M}_i) = \sum_{v \in \mathbf{V}_i} \|\sum_{\mathbf{v}' \in \mathbf{N}_v} (\mathbf{v} - \mathbf{v}')\|_2^2$. The *normal regularization* enforces smoothness of the local surface normals, i.e., neighbouring faces are expected to have similar normal direction: $\ell_{normal}(\mathbf{M}_i) = \sum_{(i,j) \in \mathbf{N}_F} (1 - \langle \mathbf{n}_i, \mathbf{n}_j \rangle)$, with \mathbf{N}_F the set of all the neighbouring faces indices, and \mathbf{n}_i the surface normal of a given face \mathbf{f}_i .

We set α , β , γ to 10.0 in our experiments. The model is trained for 200 epoches with 4 input views and batch-size 64 on 16 GPUs. We train it using Adam optimizer with initial learning rate 0.001 and decaied by 0.1 at 150, 180 epoch respectively. It takes about 6 hours to train.

A.2. Segment Retrieval Details

Single-view Segment Retrieval: To retrieve object-views for rendering in target-view, we first eliminate candidates from significantly different viewpoints (larger than 10° view changes to the target view). Then we rank the existing objects by considering their similarity in relative view angle θ and distance d from the camera.

$$score(object_{tot}, object_{src}) = |\theta_{tgt} - \theta_{src}| + 5 \cdot \max(d_{tgt} - d_{src}, 0)$$

Objects are then sampled (as opposed to a hard max) according to a categorical distribution weighted by their inverse score.

Multi-view Segment Retrieval: To retrieve object with multi views for rendering in videos and multi-cameras, we consider the view range of source object. For every object, we first calculate the view ranges overlap with the target object $\Delta\Theta$, and

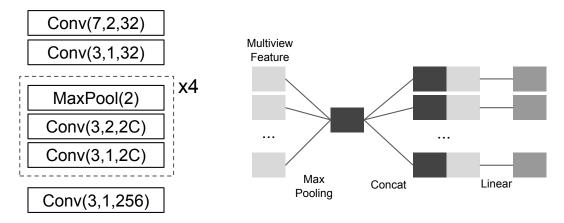


Figure 8: 3D reconstruction network architecture. Left: Image feature extraction backbone; Right: Multi-view image fusion block.

filter out source objects with small overlap ($\Delta \Theta < 20^\circ$). Then we rank the existing objects by considering their overlap and minimum distance $d_{\rm src}$ from the camera.

 $score(object_{tgt}, object_{src}) = 2 \cdot \Delta \Theta + 5 \cdot max(min d_{tgt} - min d_{src}, 0)$

Objects are then sampled (as opposed to a hard max) according to a categorical distribution weighted by their inverse score.

A.3. Depth Completion

To realistically place the simulated object in the new scene, we need to infer the occlusion relations between the simulated object and the existing scene elements. To do that, we compare the rendered depth of each simulated object's pixel with the corresponding pixel of the background scene. Since the partial LiDAR sweep belonging to the background scene is not dense enough, we first perform depth completion to generate a dense depth map for the corresponding scene. In this section, we first provide the ground-truth dense depth dataset preparation details, followed by the architectural details of the depth completion model.

Training Data Preparation: The UrbanData dataset has long trajectories of LiDAR sensor and camera sensor data with manually annotated detection labels. We first generate a dense LiDAR point cloud by aggregate the multi-sweep LiDAR sensor data. For the static background scene, we aggregate the multi-sweep data by compensating the ego-motion of the SDV. For all the objects (filtered out using the detection labels), we aggregate the multi-sweep data by transforming each of them to the corresponding object-coordinate system. For the dynamic objects, we additionally perform color-based ICP to better register the multi-sweep data. We further densify all the aggregated "vehicle" point clouds by converting each of them to a dense watertight mesh using a pre-trained implicit surface reconstruction model, DeepSDF [?]. The "non-vehilce" categories were densified by splatting each LiDAR point onto a triangular surfel disk. The aggregated point cloud is then rendered to the corresponding camera images to generate the dense depth maps. We first render the background scene aggregated points, followed by (instance-segmentation map aware) rendering of all the detected objects in ascending order of the objects median depth. We used manually annotated ground-truth instance-segmentation maps for depth map refinement.

Architecture Details: We use the generated dense-depth dataset to train a depth completion model. For the model, we use same network architecture as DeepLabV3 [11], except the first and the last convolution layers. The input to the model is a concatenated array of camera image, projected sparse depth image, projected sparse depth mask, and the dilated (dilated to 9-neighbouring pixels) sparse depth map. We initialize the DeepLabV3 architecture with the pre-trained COCO weights.

A.4. Shadow Generation Details

As we discussed in Sec. 4.2 in the paper, Fig. 9 shows the procedure that we applied to generate shadows. More qualitative comparison results on the difference between whether applied shadow generations are shown in Fig. 12.

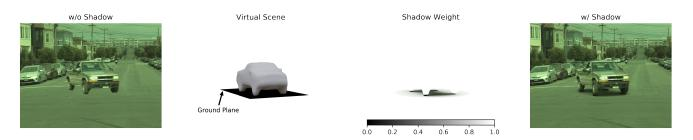


Figure 9: Schematics of Shadow Generation. (left to right): result without shadow, schematics of virtual scene, shadow weight (ratio of intensity between rendered image with inserted object and without inserted object), result with shadow

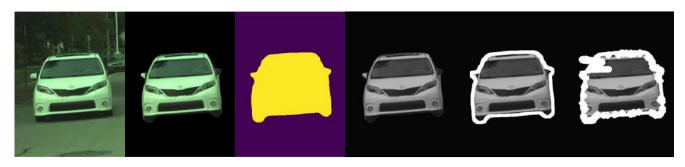


Figure 10: Input data preparation for training the synthesis network. From left to right: scene image I, object segment S and mask M and three random data augmentation including color-jitter, segment boundaries erosion-expansion and random mask in the boundary.

A.5. Post-composition Synthesis Details

Training Data Preparation: Our synthesis network is trained on dynamic object images with per-pixel instance labels inferred by [37] in the target scene. Given a scene image I, we first sample a vehicle binary mask M in that scene, as well as its corresponding RGB segment $S = I \cdot M$. Then we apply data augmentation on the segment and mask to mimic the noisy input at the inference stage, with color inconsistency, missing texture and imperfect boundary. Specifically, we applied 1) random color jitter on the scene and segment separately, which randomly changes the brightness, contrast and saturation to mimic color inconsistency between foreground and target scene; 2) random erosion on the segment boundary from 3 to 20 pixels and a random dilation on the mask M from 3 to 40 pixels to blend object boundary naturally; 3) a random drop on the segment S with 0.1%-1% of total boundary pixels and applied random dilation on those samples to mimic missing textures of the inserted virtual object. Please refer to Fig. 10 for illustration of such data augmentation process.

Architecture Details: Our synthesis network architecture is inspired by [70]. One difference is that our network takes the instance segment mask as an additional input. Thus, the network takes as input the object segment, target scene and mask region. We crop a 512×512 region centered around the object center from the full scene.

Loss Functions: We apply perceptual loss [31] on the generated image I' and I, using the conv3_3 feature activations in a pretrained VGG16 network F_v .

$$L_{G}^{\text{perc}} = \sum \|F_{v}(I) - F_{v}(G(I \cdot (1 - M^{A}), M^{A}, S^{A}))\|_{1}$$

A GAN loss is also applied to optimize the synthesis network.

 $L_G^{\text{gan}} = -\mathbb{E}_{z \sim P_z(z)}[D(G(I \cdot (1 - M^A), M^A, S^A))]$

For the discriminator, we adopt the same loss as [70].

Inference: At the inference stage during simulation, our network takes the raw composition image from novel view warping and occlusion reasoning as input and produces natural blended results. Specifically, we crop a square region with the visible rendered segment in the centre, which is twice the size of the larger side of rendered vehicles (*size*). The cropped size is set to be 128×128 at least and 1024×1024 at most. Invisible pixels due to inverse warping are filled with zeros. Then we c erode the rendered segment by $\frac{size}{64}$ pixels and dilate the mask by $\frac{size}{32}$ pixels. These inputs are fed into the synthesis network and the final outputs paste back to the original location.

A.6. Video Simulation Details

In order to simulate a realistic video footage with new dynamic objects inserted, we first select a subset of snippets from our dataset of real-world logs, each consisting of 50 consecutive frames sampled at 10Hz (for a total duration of 5s) to augment with up to 5 simulated objects using our approach.

For these relatively short sequences, we sample the object placement within the initial camera field-of-view in the first frame of the sequence and equip the object with a realistic path using the local lane graph, as illustrated in Figure 3 of the main text.

To retrieve an object for insertion from the 3D asset bank, we consider the view-range of each source object. For every object, we first calculate the view-range overlap with the target object, $\Delta\Theta$, and filter out source objects with small overlap ($\Delta\Theta < 20^\circ$). Then we rank the existing objects by considering their overlap and minimum distance $d_{\rm src}$ from the camera.

$$score(object_{tot}, object_{src}) = 2 \cdot \Delta \Theta + 5 \cdot max(min d_{tet} - min d_{src}, 0)$$

Objects are then sampled (as opposed to a hard max) according to a categorical distribution weighted by their inverse score.

We now describe how we use a set of heuristics-based behavior and lateral/longitudinal driving models to refine the path into a timestep-by-timestep *trajectory* of *kinematic states* comprising of location, orientation, velocity, and acceleration. This realistic trajectory simulation helps the added vehicle in the simulated video achieve realistic motion such as braking and acceleration. After executing segment retrieval and performing a final collision check, the object and its refined trajectory is then inserted into the log for inclusion. Additional objects can be added in a similar fashion.

We use a cost-based heuristic behavior model for determining lane change actions, a heuristic lateral model for the side-to-side motion of the object, and the Intelligent Driver Model [59] for the longitudinal movement. We define the following notation:

 p_x = longitudinal position v_x = longitudinal velocity p_y = lateral position v_y = lateral velocity.

All models use a frequency, or reaction time, of 10Hz.

Behavior Model Details: Two actors are considered as colliding if the inter-vehicle distance between them is less than 2m. Let d_h , d_f denote the distances between the given vehicle and the headway (nearest front) vehicle or following (nearest back) vehicle respectively. Similarly, define c_h , c_f to be the headway and following costs. The cost functions we use are:

$$c_h = \begin{cases} 10^8 & d_h < 2\\ \frac{10^4}{d_h} & \text{otherwise} \end{cases}$$
$$c_f = \begin{cases} 10^8 & d_f < 2\\ \frac{10^2}{d_f} & \text{otherwise.} \end{cases}$$

The cost of making a lane change is 10^3 , and the cost c_l for being close to the end of a lane when distance d_l from the lane end is

$$c_l = \frac{10^5}{d_l}.$$

Dataset Split	#Logs	#Frames used
Split A	5K	1.2M
Split B	7K	7K
Split C	2.8K	2.8K
Split D	2K	2K

Table 5: UrbanData dataset splits.

Task	SubTask	Dataset Split	Label Used
GeoSim	Mesh Reconstruction training	Split A	3D Box and mask from [37]
GeoSim	Post-Compostion training	Split A	mask from [37]
GeoSim	Depth Completion training	Split B	Aggregated Lidar
GeoSim	Whole pipeline	Split C	3D Box from [43]
Baselines	Training	Split B	GT Semantic Mask
Baselines	Test	Split C	GT Semantic Mask
Downstream	Sim2Real Training	Split C	GT Semantic mask and GeoSim Mask
Downstream	Sim2Real Evaluation	Split D	GT Semantic mask

Table 6: UrbanData Experimental setting.

Lateral Model Details: We use a simple heuristic for the target lateral speed that seeks to return to the lane centerline, bounded by a function of the longitudinal (forward-backward) movement. Specifically,

$$v_x = \min(-p_x, 0.1v_y).$$

clipped so that the maximum acceleration magnitude is 3ms^{-2} .

Longitudinal Model Details: We use the following parameters: minimum and maximum target speeds of 15ms^{-1} and 25ms^{-1} respectively, acceleration exponent of 4ms^{-2} , maximum acceleration and deceleration magnitudes of 5ms^{-2} , minimum gap of 2m, headway time of 1.5s, and default vehicle length of 4.5m.

A.7. UrbanData Dataset breakdown

In the UrbanData, we have roughly 16.5K labelled snippets. Out of these, 12K snippets have manually annotated 2D segmentation maps (one frame per snippet). As shown in Tab. 5, we divide these 16.5K snippets into multiple splits for training and testing various components of the GeoSim pipeline as well as the baslines. Tab. 6 maps each task to its corresponding training/ testing dataset split. Note that GeoSim does not need any gt labeled data. All labeled data are for training/evaluation purposes.

A.8. A/B interface and instructions

As discussed in Section 5.2 of the main paper, we performed a human study to demonstrate that GeoSim images appear more realistic compared to other baseline methods. For interface simplicity and ease of annotation, we performed pairwise comparisons instead of ranking. We also perform pair-wise comparison over ranking to mitigate user-bias, as all the baselines we compare against use the same object proposal method. An example interface is shown in Fig. 11. Each user would be provided two images, one generated with GeoSim and one generated with one of the baseline methods. Each image would be assigned with equal probability to the top or bottom location. Both the baseline and GeoSim would receive the same input real image and semantic segmentation. Based on the method and placement procedure, an object would be added to the scene, not necessarily in the same location (as seen in Fig. 11). We asked 13 users who are familiar with self-driving but who had limited or no knowledge of image simulation or of our method to select which image they prefer. On average, users annotated approximately 115 images, for a total of ~1500 images. Here are the detailed instructions we provided along with each query: Detailed instructions:

For each pair of images, please select the more realistic of the two by selecting either TOP or BOTTOM as the image label. Make sure to consider all relevant aspects of realism including but not limited to: visual appearance, lighting, shadows, relationship between elements within the image (ie occlusions), consistency in color, weather conditions, positioning on the road, and traffic regulations. We recommend clicking either on the images or on the top left blue arrow button to resize both images to fit the window. Click "next task" to move on. Note you will not be able to go back to a previous image, and the "Finish" button has no effect until all examples have been labeled, so there is no risk in accidentally clicking it. You can use the keyboard shortcuts 1,2 for TOP, BOTTOM, respectively.

We compute the success rate, i.e. whether our method is preferred over a specific baseline as: $\frac{\# \text{ of times GeoSim selected}}{\# \text{ of pairs with GeoSim and baseline}}$.



Figure 11: A/B Test User Interface. Users must select which image ("TOP" or "BOTTOM") they consider most realistic.

B. Qualitative Results

B.1. Visual Comparisons

In addition to the qualitative results shown in Fig. 5 in the paper, we further showcase more qualitative comparisons among the previously-discussed image simulation baselines in Fig. 12. As can be seen from Fig. 12, GeoSim produces much more realistic and 3D aware simulated images, compared to the visually significant failures (e.g., blurred textures, implausible placements, distorted shapes, boundary artifacts) produced by the other simulation methods. We also showcase more qualitative comparisons on public dataset Argoverse in Fig. 13.

B.2. Ablation Analysis

We also conduct qualitative ablation on three key components in post processing: occlusion reasoning, shadow and synnet. We compare GeoSim results against the one with the selected component removed. As seen in Fig. 15, with any one of the component being removed, the realism of the synthesis results drop significantly. Removing occlusion reasoning, the synthesized vehicles aren't able to conform with the existing scene elements. Removing Shadow, the synthesized vehicles seems to be off-the ground. Removing synnet, the synthesized vehicles show inconsistent illumination and color-balancing w.r.t the target scene and discrepancies at the boundaries. Please zoom in to see the detail.

B.3. Failure Cases

While GeoSim simulated images manages to produces photo-realistic results in many cases, there is still space for potential improvements. In Fig. 14, we highlight four major failure cases: (1) Incorrect Occlusion Relationships in complicated scene, (2) Irregular reconstructed mesh, (3) Inaccurate object poses, usually caused by Map error and (4) Illumination failure by distinct illumination difference between rendered segment and target scene.

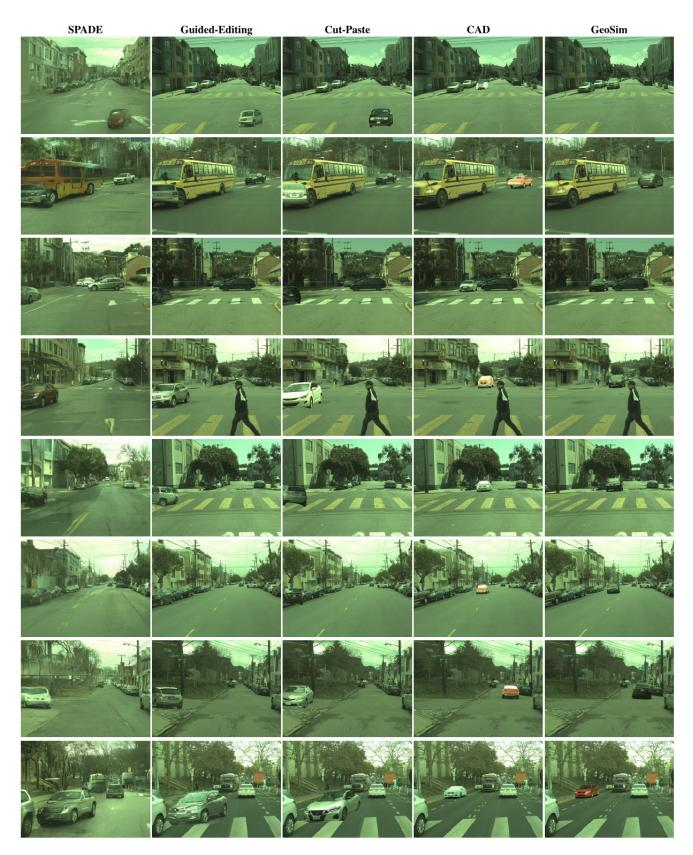


Figure 12: Qualitative Comparison of Image Simulation approaches.

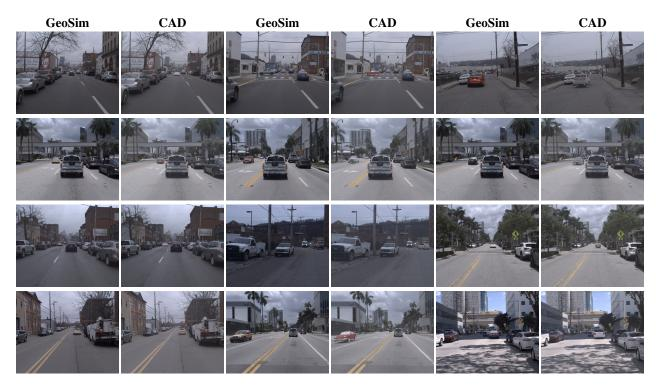


Figure 13: Qualitative Comparison of Image Simulation approaches on Argoverse.

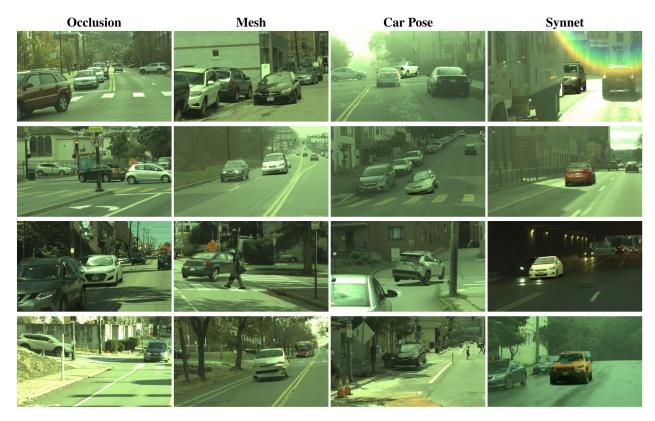


Figure 14: Qualitative visualization of the failure cases.

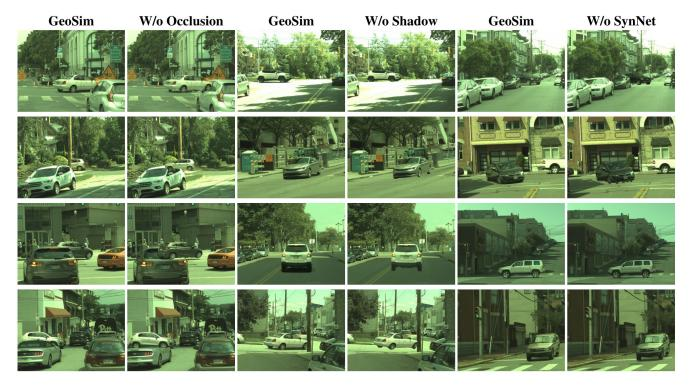


Figure 15: Qualitative Ablation on the composition.